A Local Threshold Checkerboard Algorithm for Adaptive Optics System With a Plenoptic Sensor

Zhichong Wang , Tao Chen, Xudong Lin, Liang Wang , Qichang An , and Jintian Hu

Abstract—Adaptive optics systems will encounter challenges under strong atmospheric turbulence conditions. Recently, a modified approach based on plenoptic sensor has attracted considerable attention. However, after wavefront correction under strong turbulence, we found that the existing wavefront reconstruction algorithm has difficulty in accurately reconstructing the residual aberrations. Therefore, we proposed a local threshold checkerboard algorithm to improve the accuracy of wavefront reconstruction by thresholding specific areas of central sub-apertures of the plenoptic sensor. In order to demonstrate the effectiveness of our algorithm, we designed and built an experimental platform. The platform included a deformable mirror, which we were able to adjust to simulate several different aberration conditions. Afterwards the direct-gradient method was used for correction of the residual aberrations, which were reduced to less than 0.1λ(RMS), demonstrating the effectiveness of our algorithm.

Index Terms—Atmospheric turbulence, plenoptic sensor, wavefront correction, wavefront reconstruction.

I. INTRODUCTION

ADAPTIVE Optics has been widely used in astronomical imaging, laser communications and other fields [1]–[3]. Nowadays the most frequently-used wavefront sensor is Shack-Hartmann (S-H) wavefront sensor, which works well under weak

Zhichong Wang and Jintian Hu are with the Changchun Institute of Optics, Fine Mechanics and Physics, Chinese Academy of Sciences, Changchun 130033, China, and also with the University of Chinese Academy of Sciences, Beijing 100049, China (e-mail: 1250738690@qq.com; 937472452@qq.com).

Tao Chen and Qichang An are with the Changchun Institute of Optics, Fine Mechanics and Physics, Chinese Academy of Sciences, Changchun 130033, China (e-mail: chent@ciomp.ac.cn).

Xudong Lin is with the Changchun Institute of Optics, Fine Mechanics and Physics, Chinese Academy of Sciences, Changchun 130033, China, and also with the MOE Key Laboratory of TianQin Mission, TianQin Research Center for Gravitational Physics & School of Physics and Astronomy, Frontiers Science Center for TianQin, Gravitational Wave Research Center of CNSA, Sun Yat-sen University (Zhuhai Campus), Zhuhai 519082, China (e-mail: 13039222921@126.com).

Liang Wang is with the Changchun Institute of Optics, Fine Mechanics and Physics, Chinese Academy of Sciences, Changchun 130033, China, and also with the School of Mechanical and Aerospace Engineering, Jilin University, Changchun 130012, China (e-mail: wangliang.ciomp@foxmail.com).

Digital Object Identifier 10.1109/JPHOT.2021.3138776

turbulence conditions. However, it is challenged under strong turbulence conditions with some severe problems [4], which affect wavefront reconstruction and correction.

Several different methods have been proposed to get this difficulty solved. An approach based on a light field camera for reconstructing wavefront is one alternative scenario, which measures every micro-lens image to reconstruct the distorted wavefront [5], [6]. And on this basis researchers from the University of Maryland College Park have proposed a modified plenoptic sensor for wavefront reconstruction [7]–[15], which can obtain the intensity and angular information of the distorted wavefront simultaneously. An algorithm called checkerboard algorithm has been proposed by researchers to reconstruct the disturbed wavefront [16]. However, after using the checkerboard algorithm to perform wavefront reconstruction under strong turbulence conditions, it was found that RMS of the residual aberrations is more than 0.25λ, which demonstrates that checkerboard algorithm has difficulty accurately reconstructing the residual aberrations, and the accuracy of the wavefront reconstruction cannot be guaranteed.

In the current study, a local threshold checkerboard (LTC) algorithm is proposed to improve the accuracy of wavefront reconstruction of the plenoptic sensor by thresholding specific areas of the central sub-apertures of a plenoptic sensor. The direct-gradient method is then used for correction of distorted wavefront.

We introduce the principles of a plenoptic sensor we used in Section II. Then the checkerboard algorithm and its limitation are discussed and the LTC algorithm is proposed as an alternative. In Section III we present the experimental results, and the direct-gradient method is used for wavefront correction. Finally we summarize the conclusions in Section IV.

II. MATERIALS AND METHODS

A. Principles of the Plenoptic Sensor

The structure of a plenoptic sensor is shown in Fig. 1. A plenoptic sensor consists of an objective lens, a micro lens array (MLA) and an image sensor. In Fig. 1, d_o and f_o are used to represent the diameter and focal length of the objective lens, d_M and f_M are used to represent the pitch and focal length of MLA.

According to Fourier optics, the objective lens performs the first two-dimensional Fourier transform on wavefront $t_1(x, y)$ to the transformed wavefront $t_2(u, v)$. The MLA performs a second two-dimensional Fourier transform on the wavefront $t_2(u, v)$ to the transformed wavefront $t_3(s, t)$. These two transforms are
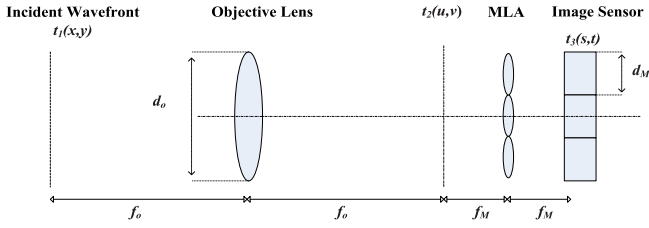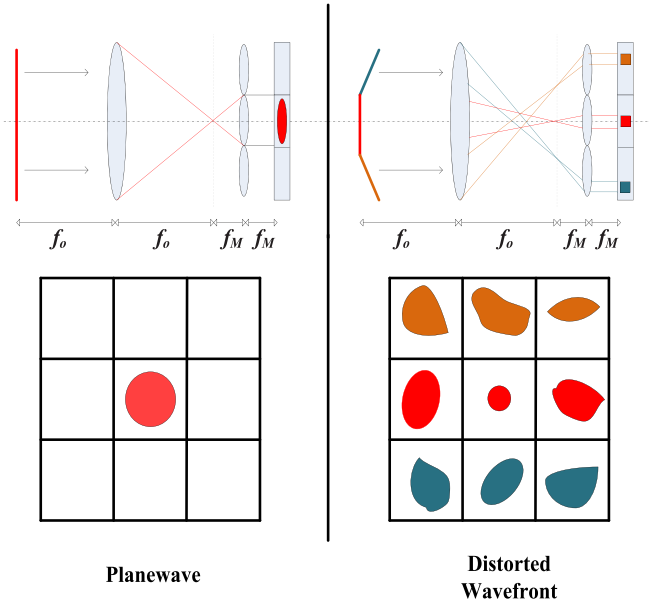
Fig. 1. Structure of the plenoptic sensor.

Fig. 2. Imaging schematic of the plenoptic sensor.

Fig. 3. Diagram of the checkerboard division and imaging of plane wave.

expressed as:

$$t_2(u,v) = \frac{1}{j\lambda f_o} \int \int t_1(x,y) \exp\left\{\frac{-j2\pi}{\lambda f_o}(ux+vy)\right\} dxdy \tag{1}$$

$$t_3(s,t) = \frac{1}{j\lambda f_M} \int \int t_2(u,v) \sum_{X,Y} rect\left(\frac{u+s-2Xd_M}{d_M}\right)$$

$$rect\left(\frac{v+t-2Yd_M}{d_M}\right)$$

$$\exp\left\{\frac{-j2\pi}{\lambda f_M}(u-Xd_M)(s-Xd_M)+(v-Yd_M)(t-Yd_M)\right\}$$

$$dudv \tag{2}$$

where the coordinates of MLA lens are expressed by (X, Y) in (2). Besides, the f-number of the MLA should not be greater than the f-number of the objective lens so as to avoid overlapping between MLA sub-images [14], [17], which can be expressed as:

$$\frac{d_o}{f_o} \le \frac{d_M}{f_M} \tag{3}$$

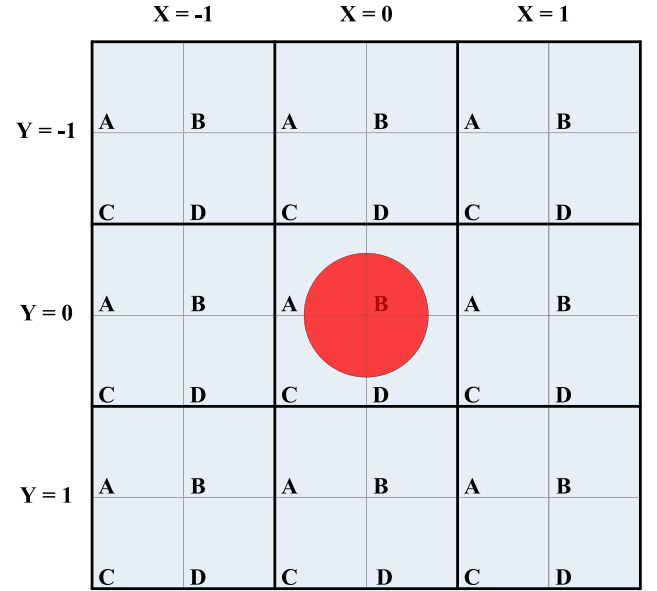Fig. 2 shows the imaging of the plenoptic sensor. If the incident wavefront has no distortions, it will only be imaged

by the central MLA unit. If the incident wavefront is distorted, however, the beam will be dispersed into each MLA sub-aperture on the basis of the angular spectra of the incident wavefront [14].

B. Wavefront Reconstruction

1) Checkerboard Reconstruction Algorithm and Its Limitation:

a) Algorithm: The wavefront reconstruction algorithm we use is called the checkerboard reconstruction algorithm [16]. The principle of the checkerboard reconstruction algorithm is to divide each MLA unit into different "checkerboard" units. These checkerboard units are then also divided in each MLA sub-aperture, and each checkerboard unit represents different spatial positions of the incident wavefront.

There are 3×3 MLA units in Fig. 3, four different checkerboard units are divided in each MLA unit and designated as "A," "B," "C," and "D," respectively, and several pixels are included in each checkerboard unit. Each unit "A" in each sub-aperture represents the same angular information of the incident wavefront. Unit "B", "C", and "D" have similar representation. If the incident wavefront in Fig. 3 is a plane wave, it is only imaged by the central MLA unit.

The process of checkerboard reconstruction algorithm is described in Fig. 4. If the incident wavefront is distorted, it is separated into different MLA units, which is shown in the left-hand image of Fig. 4. When reconstructing the wavefront, using unit "A" as an example, a search is conducted in all unit "A" and the MLA sub-aperture coordinates (X, Y) determined of the unit "A" with the highest number of pixels. The coordinate (-1,0) in Fig. 4, is expressed as the spatial information of incident wavefront at the corresponding position (unit "A") as shown in the right-hand image in Fig. 4. The same operation is conducted for "B," "C," and "D." After acquiring all of the (X, Y) coordinates, the corresponding wavefront gradient vector (α, β) can be obtained
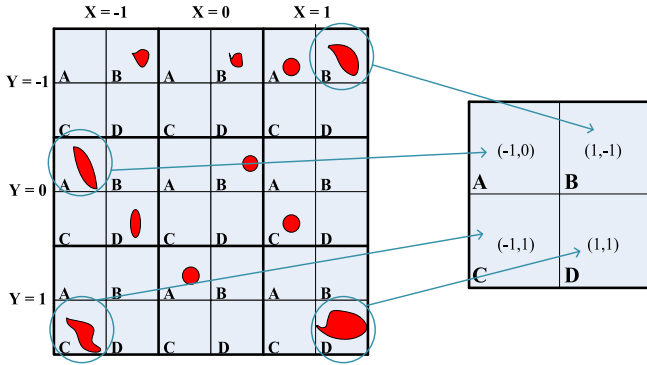
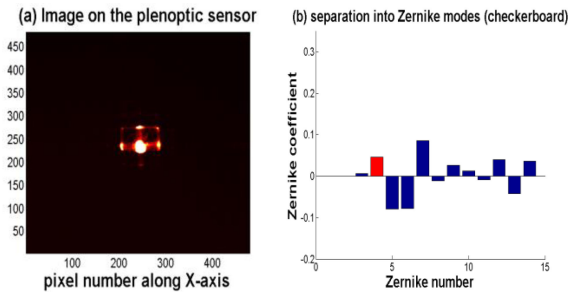Fig. 4. Diagram of the checkerboard reconstruction.

Fig. 5. Residual aberration (a) plenoptic imaging, and (b) Zernike polynomials reconstructed by the checkerboard algorithm.

using Eq. (4):

$$(\alpha, \beta) = \frac{2\pi d_M}{\lambda f_o}(X, Y) \tag{4}$$

b) Limitation: It can be seen from the foregoing that when the incident wavefront is a plane wave, it is only imaged by the central MLA unit. According to Eq. (4), the coordinates of the imaging MLA units (X, Y) are $(0, 0)$, and the calculated wavefront gradients are 0. However, when the plenoptic sensor corrects the strong atmospheric turbulence and there are residual aberrations remaining, the incident beam is mostly concentrated in the central MLA sub-aperture. At this time, the coordinates of the MLA unit (X, Y) calculated by the checkerboard algorithm are mostly $(0, 0)$, so the wavefront gradients calculated by Eq. (4) will be very small, even close to the plane wave, which is different from the actual situation.

For example, Fig. 5(a) shows a residual aberration imaging of the plenoptic sensor, in which there is a 0.3 λ Defocus type of aberration remaining. If the checkerboard algorithm is used to reconstruct the wavefront in Fig. 5, according to the above analysis, the reconstructed Zernike coefficient is smaller, which is shown in Fig. 5(b). If the plenoptic sensor cannot perform accurate wavefront reconstruction for residual aberrations, it will affect the accuracy of the wavefront correction of the system.

2). Local Threshold Checkerboard Reconstruction Algorithm:

a) Algorithm: In order to make the accuracy of wavefront reconstruction improved, an LTC algorithm is proposed, which

---

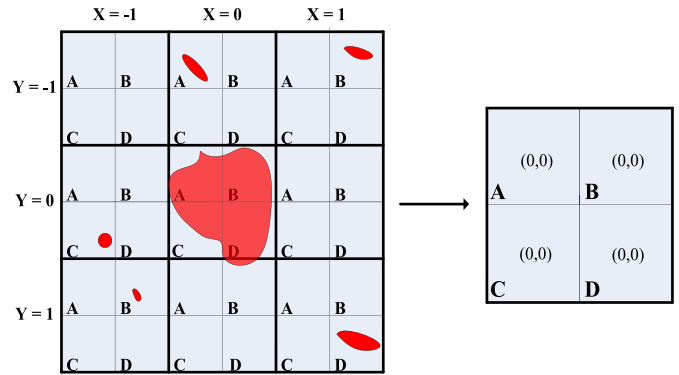| **Algorithm:** LTC algorithm |
| --- |
| **Input:** a plenoptic image, *Input* (x, y) |
| **Output:** the reconstructed wavefront image, *Output* (x, y) |
| 1: Select the sub-apertures corresponding to the 3×3 MLA units centered on the central MLA unit. |
| 2: Some specific areas of the central sub-aperture are set to 0. |
| 3: **for** every checkerboard unit |
| 4: Obtain the coordinates of (X, Y) by using the checkerboard algorithm. |
| 5: **end for** |
| 6: Calculate the gradients of incident wavefront through (X, Y). |
| 7: Reconstruct the incident wavefront using the gradients information. |

Fig. 6. Diagram of the residual aberration reconstruction using checkerboard algorithm.

can reconstruct residual aberrations that are difficult to accurately reconstruct using the checkerboard algorithm. The principle of the LTC algorithm is as follows. First, the sub-apertures corresponding to the 3×3 MLA units centered on the central MLA unit are selected. A threshold operation is then performed, in which some specific areas of the central sub-aperture of the plenoptic sensor are set to 0. Finally, the checkerboard algorithm discussed above is used to calculate the wavefront gradient. After calculation by the LTC algorithm, the coordinates of the MLA unit (X, Y) corresponding to the offset areas will change from 0 to ± 1, the corresponding wavefront gradients will become non-zero values, thereby amplifying the reconstruction result of the original algorithm, and achieving the purpose of improving the reconstruction accuracy. The overall process is shown below:

As an example, a 3×3 MLA unit is shown in Figs. 6 and 7, and four checkerboard units are divided in each MLA unit as "A," "B," "C," and "D". There are some residual aberrations remaining in Figs. 6 and 7, and the incident beam is mostly concentrated in the central MLA. At this time, in Fig. 6 the coordinates calculated by the checkerboard algorithm are $(0, 0)$, which will produce a substantial wavefront reconstruction error.
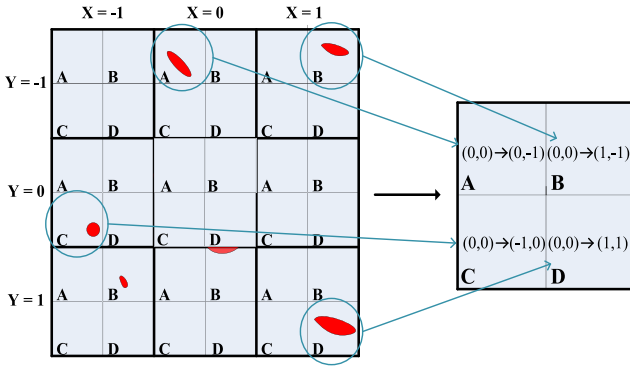
Fig. 7.   Diagram of the residual aberration reconstruction using LTC algorithm.
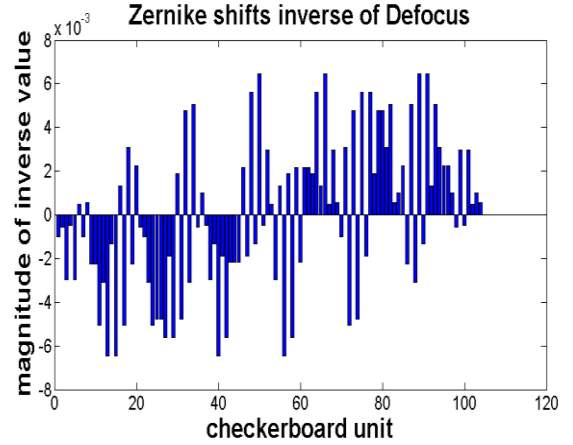

Fig. 8.   Zernike shifts inverse vector histogram of Defocus aberration.

Fig. 9.   Wavefront reconstruction errors under different thresholds of Defocus aberration.

Fig. 7 shows the process of the LTC algorithm. For example, the checkerboard units "A," "B," "C," and "D" of the central MLA unit are set to 0. Subsequently, after calculating the co-ordinates (X, Y), compared with the results of checkerboard algorithm, the corresponding coordinates have become non-zero, which amplifies the reconstruction result of the checkerboard algorithm.

b) Computational Complexity: As we discussed before, the differences between LTC algorithm and checkerboard algorithm are number of MLA sub-apertures and thresholding operation. It takes little time to perform thresholding operation when using LTC algorithm, so when comparing the computational complexity of these two algorithms, all we should consider is the number of MLA sub-apertures, which will affect the iteration times of the algorithms.

Based on the discussion above, the computational complexity of LTC algorithm can be simplified as that of the iteration of LTC algorithm, so does checkerboard algorithm. The complexity of LTC algorithm is $O(n_{LTC}^2)$, where n_{LTC} is 3. The complexity of checkerboard algorithm is $O(n_{check}^2)$, where n_{check} is 15 in our study. Obviously, LTC algorithm has lower computational complexity. In other words, compared with checkerboard algorithm, LTC algorithm is less time-consuming when reconstructing residual aberrations.

c) Selection of Offset Areas: Using the Defocus aberration as an example, the blue histogram of Fig. 8 is the Zernike pseudo-inverse vector corresponding to the Defocus aberration. This vector is multiplied by the wavefront gradient to calculate the Zernike coefficient of the Defocus aberration using Eq. (5):

$$a = Z^+ * G \qquad (5)$$

where a represents the Zernike coefficient, Z^+ is the Zernike pseudo-inverse vector, and G is the wavefront gradient.

Here is the criteria of the selection of thresholding checker-board areas: suppose there is the Defocus aberration of Fig. 5 remaining, when performing thresholding operations, firstly, we take the absolute values of the elements of the vector in Fig. 8; secondly, we take the first 30% of the absolute values as thresh-olds, for they have greater effect on wavefront reconstruction; finally, we determine the coordinates of thresholding checker-board areas, which are corresponding abscissas of the thresholds.
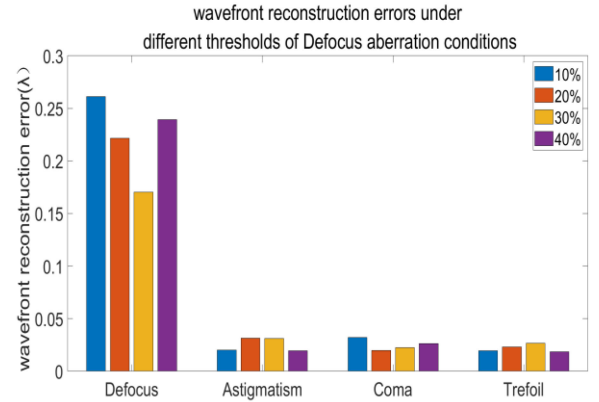
The same operations are performed when reconstructing other aberrations. The selection of the offset areas can only affect the main aberrations and cannot affect the reconstruction of other aberrations. We compared the reconstruction errors of Defocus aberration under different thresholds conditions, the result was shown in Fig. 9, and reconstruction errors of other aberrations when threshold of Defocus aberration changes were also shown in Fig. 9. As can be seen, when reconstructing aberrations, 30% works best. Besides, wavefront reconstruction errors of other aberrations change little when threshold of Defocus aberration changes, demonstrating that the selection of the offset areas doesn't affect the reconstruction of other aberrations. The results of wavefront reconstruction are listed below.

C. Experiments Based on Plenoptic Sensor

To verify the effectiveness of the LTC algorithm, an exper-imental platform was designed and built. The schematic and actual experimental layout of the platform are shown in Figs. 10 and 11. A 633 nm laser goes through Beam Splitter1 into Lens1 to create a parallel beam that spreads to a 21-element deformable mirror, the layout of which is shown in Fig. 12. By adjusting the deformable mirror, the distorted beam reflects and goes through
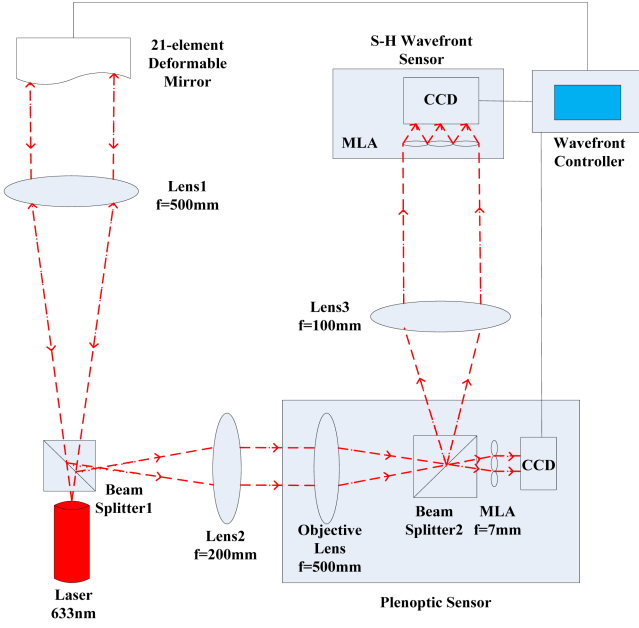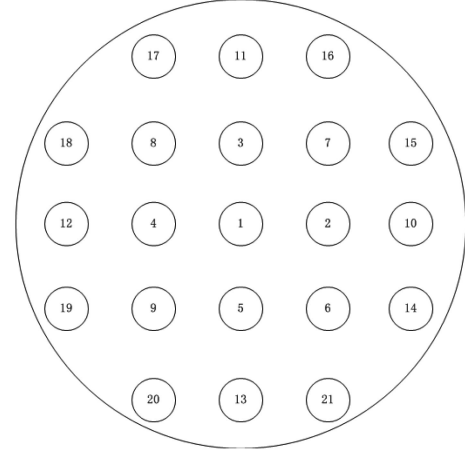
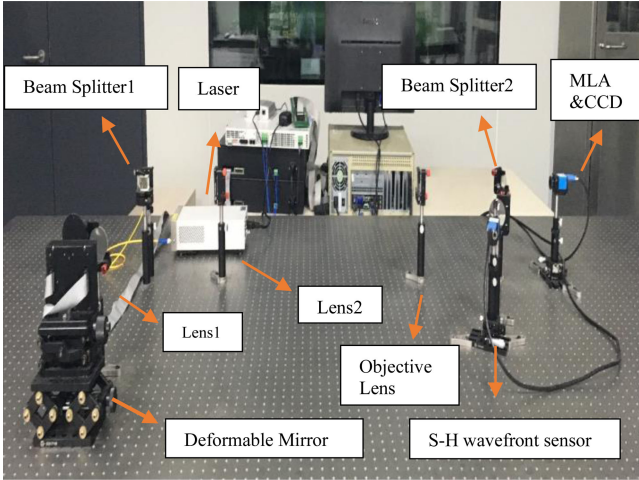Fig. 10. Schematic of the experimental platform.

Fig. 11. Actual experimental layout.

Lens1 and Lens2 as a shrink-beam group. Part of the incident beam passes through Beam Splitter2 through Lens3 into the S-H wavefront sensor as a comparison with the plenoptic sensor. The remaining incident beam goes to the plenoptic sensor.

The MLA of the plenoptic sensor was 15×15, and the focal length and the pitch of each MLA unit are 7mm and 0.2mm. 64 checkerboard units were divided in each MLA sub-aperture, and the size of each checkerboard unit was 2×2 pixels. The focal length of objective lens was 500 mm, according to Eq. (3), the width of incident beam should not be greater than 14 mm. So we used the shrink-beam group to satisfy the restriction, and the focal lengths of Lens1 and Lens2 were 500 mm and 200 mm.

The MLA of the S-H wavefront sensor we used was 13×13 units, and the number of valid sub-apertures was 137.

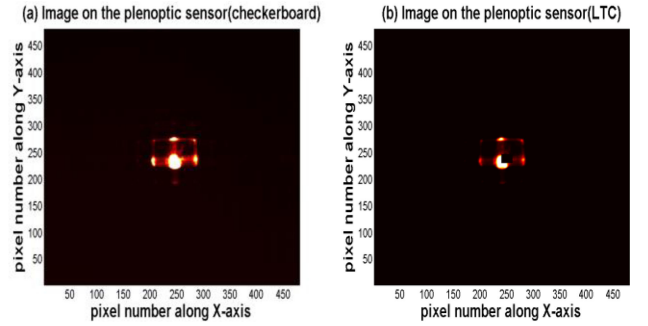Fig. 12. Layout of 21-element deformable mirror actuators.

Fig. 13. Plenoptic sensor image using (a) checkerboard algorithm, and (b) LTC algorithm.

III. RESULTS AND DISCUSSION

A. Wavefront Reconstruction

Several different Zernike aberrations can be generated by adjusting the control voltage of the deformable mirror actuators. The aberrations used in experiments are expressed as:

$$Defocus : Z_2^0(r,\theta) = \sqrt{3}(2r^2 - 1) \tag{6}$$

$$Astimatism : Z_2^2(r,\theta) = \sqrt{6}r^2 \sin(2\theta) \tag{7}$$

$$Coma : Z_3^1(r,\theta) = \sqrt{8}(3r^2 - 2r) \sin\theta \tag{8}$$

$$Trefoil : Z_3^3(r,\theta) = \sqrt{8}r^3 \sin(3\theta) \tag{9}$$

where (r, θ) represent the normalized radius and angle. In order to demonstrate the effectiveness of the LTC algorithm, we used the checkerboard algorithm and the LTC algorithm to perform wavefront reconstruction on the aberrations listed above, which is referenced by S-H wavefront sensor. The coefficient of each aberration was 0.3 λ.

Using the Defocus aberration as an example, the corresponding histogram of the Zernike coefficient is colored red. Fig. 13(a) shows the plenoptic sensor image when using the checkerboard algorithm, and Fig. 13(b) shows the image when using the LTC algorithm, where some pixel values in the partial area of the
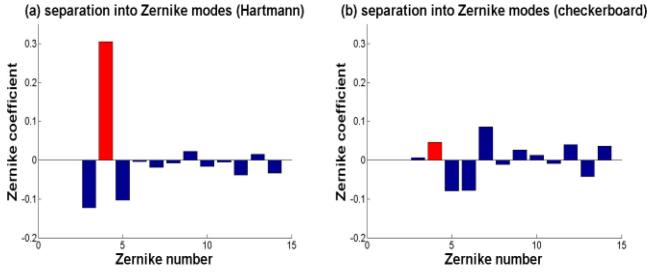
Fig. 14. Wavefront reconstruction result of (a) S-H wavefront sensor, and (b) checkerboard algorithm.
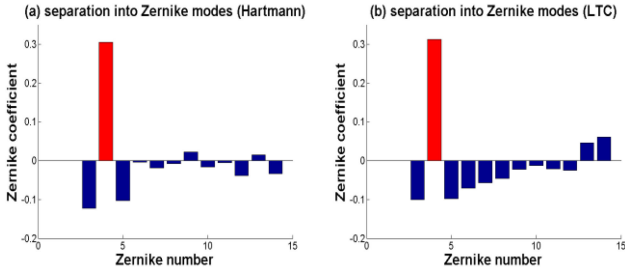

Fig. 15. Wavefront reconstruction result of (a) S-H wavefront sensor and (b) LTC algorithm.
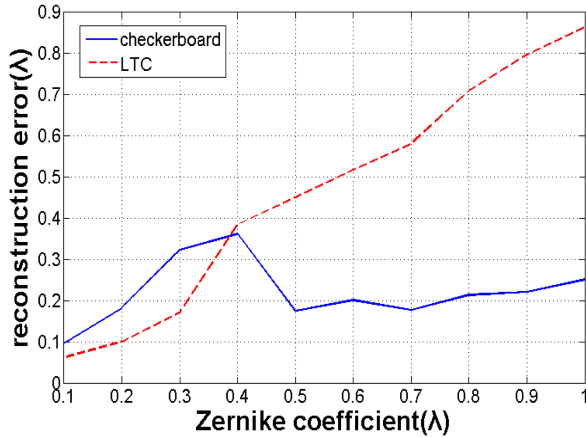

Fig. 16. Wavefront reconstruction error of Defocus aberration under different Zernike coefficients.

central sub-aperture are set to 0. Fig. 14 shows the comparison of wavefront reconstruction results between the S-H wavefront sensor and the checkerboard algorithm, where Fig. 14(a) is the wavefront reconstruction of the S-H wavefront sensor, and Fig. 14(b) is the reconstruction of the checkerboard algorithm. As can be seen, the coefficient reconstructed by the checkerboard algorithm was less than 0.1, and the error of reconstruction was large. Fig. 15 (a) and (b) show the comparison between the wavefront reconstruction results of the S-H wavefront sensor, and that of the LTC algorithm, respectively. Obviously, the result of the LTC algorithm is closer to the result of the S-H wavefront sensor, and results in a lower error.

Table I shows four different wavefront reconstruction errors of the two algorithms. The RMS of wavefront reconstruction

TABLE I
WAVEFRONT RECONSTRUCTION ERRORS OF TWO ALGORITHMS

Aberration	Trefoil	Coma	Astigmatism	Defocus
RMS of checkerboard	0.1911λ	0.3082λ	0.2610λ	0.3227λ
RMS of LTC	0.1403λ	0.1855λ	0.1611λ	0.1702λ

error is calculated as follows:

$$RMS = \sqrt{\sum_{i=1}^{n} \left(Z_{rec}(i) - Z_{input}(i)\right)^2} \qquad (10)$$

where Z_{input} represents the input Zernike coefficients, and Z_{rec} represents the reconstructed Zernike coefficients of different aberrations. As can be seen, in all instances the RMS of the LTC algorithm is less than the RMS of the checkerboard algorithm, which demonstrates that the LTC algorithm is proven effective for acquiring a higher reconstruction accuracy.

We also compared the wavefront reconstruction errors of these aberrations of two algorithms under different Zernike coefficients conditions. The result of Defocus aberration is shown in Fig. (16). As can be seen, when coefficients were smaller than 0.3λ, due to the limitation of checkerboard algorithm we discussed, wavefront reconstruction error of checkerboard algorithm was greater than that of LTC algorithm; with the increase of coefficients, incident beam was dispersed into more MLA sub-apertures, LTC algorithm didn't perform as well as checkerboard algorithm. The results of other aberrations are similar to that of Defocus aberration. The results can also demonstrate the effectiveness of LTC algorithm for acquiring a higher reconstruction accuracy.

Besides, we compared the average speed for reconstructing residual aberrations of these two algorithms. Due to the smaller number of MLA sub-apertures LTC algorithm use, the average running time of LTC algorithm is 0.012s, less than that of checkerboard algorithm, which is 0.026s. The result of average speed demonstrates the correctness of the analysis of the computational complexity of these two algorithms.

B. Wavefront Correction

1) Single Aberration Correction: To demonstrate the effectiveness of the LTC algorithm, we first used the checkerboard algorithm and the LTC algorithm to perform closed-loop experiments on four different single aberrations described in Eqs. (6)–(9). The direct-gradient method was used for wavefront correction, which can calculate the control voltage of each actuator of the deformable mirror according to the wavefront gradients reconstructed by the plenoptic sensor [18]–[20]. The coefficient of each aberration was 3 λ.

Using the Defocus aberration as an example, the wavefront correction result using the checkerboard algorithm is shown in Fig. 17, where Fig. 17(a) shows the plenoptic sensor imaging of the Defocus aberration before correction, and Fig. 17(b) shows that after correction. Most of the incident beam was
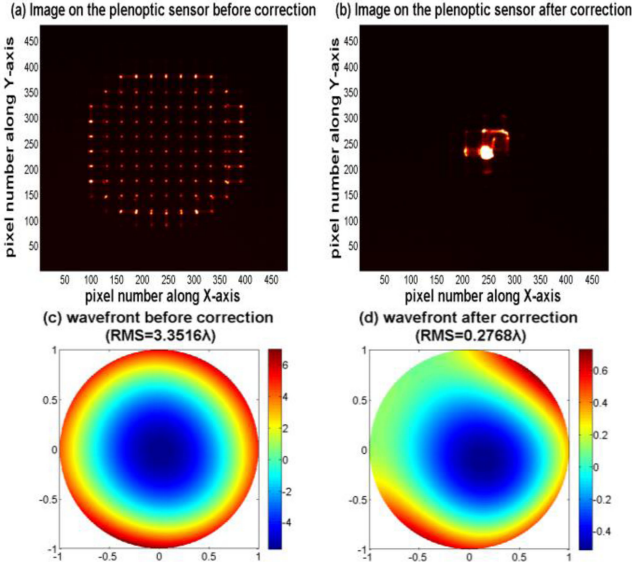
Fig. 17. Wavefront correction result of Defocus aberration using checkerboard algorithm.

Fig. 18. Residual wavefront correction result using LTC algorithm.

TABLE II
RESIDUAL ERRORS OF SINGLE ABERRATION CORRECTION TWO ALGORITHMS

Aberration	Trefoil	Coma	Astigmatism	Defocus
RMS of checkerboard	0.2598λ	0.3541λ	0.3211λ	0.2768λ
RMS of LTC	0.0822λ	0.0875λ	0.0945λ	0.0903λ

TABLE III
STREHL RATIO AFTER CORRECTION OF TWO ALGORITHMS

Aberration	Trefoil	Coma	Astigmatism	Defocus
checkerboard	0.376	0.301	0.322	0.356
LTC	0.754	0.742	0.705	0.721

concentrated in the central MLA sub-aperture, and Strehl ratio was improved from 0.061 to 0.356 after correction with checkerboard algorithm. Fig. 17(c) and (d) show the wavefront before and after correction, the wavefront RMS values before and after correction are 3.3516 λ, and 0.2768 λ, respectively, and the P-V values are 18.2055λ, and 1.2633 λ, respectively, which means that most of the Defocus aberration was corrected. However, there still remained 0.25 λ of the Defocus aberration. Due to the limitation of the checkerboard algorithm discussed above, it is difficult to correct the residual aberrations using the checkerboard algorithm.

To further improve the accuracy of wavefront correction, after the closed-loop correction of the Defocus aberration, the LTC algorithm and the direct-gradient method were used to reconstruct and correct the residual aberrations. The comparison of the plenoptic sensor imaging is shown in Fig. 18, where Fig. 18(a) is the plenoptic sensor imaging before correction, and Fig. 18(b) is the one after correction. More incident beam was concentrated in the central MLA sub-aperture, and Strehl ratio was improved from 0.356 to 0.721 after correction with LTC algorithm. Fig. 18(c) and (d) show the wavefront before and after correction, the wavefront RMS values before and after correction are 0.2768 λ, and 0.0903 λ, respectively, and the P-V values are 1.2633 λ and 0.8425 λ, respectively. After using the LTC algorithm, the residual aberration is further reduced, and a higher correction accuracy is obtained with our algorithm.
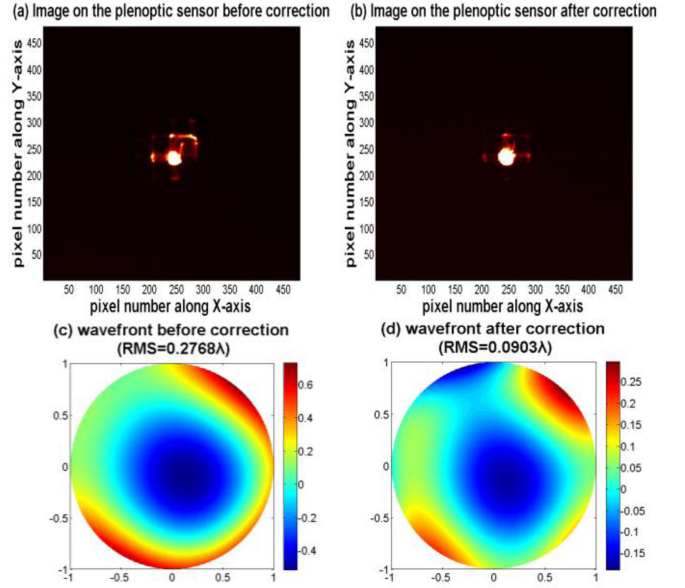
Tables II and III shows residual errors of four single aberration correction and comparison of Strehl ratio of the two algorithms. As can be seen, after using the LTC algorithm, the RMS of the single wavefront correction is further reduced, Strehl ratio is further improved, demonstrating that a higher correction accuracy can be acquired with the LTC algorithm.

2) Strong Turbulence Correction: To demonstrate the effectiveness of the LTC algorithm, we used the checkerboard and LTC algorithms to perform closed-loop experiments on aberrations caused by strong atmospheric turbulence. The direct-gradient method was used for wavefront correction.

A method based on Zernike polynomials is used to simulate strong atmospheric turbulence [21]. A set of random Zernike coefficients under strong atmospheric turbulence can be acquired using Eq. (11):

$$a = U^T \cdot B \cdot \left(\frac{D}{r_0}\right)^{\frac{5}{6}} \tag{11}$$

where a represents the Zernike coefficients, U is the transition matrix, B is the vector which the components are Gaussian random variables, D represents the diameter of the main lens of the optical system, r0 is the Fried coherence length. The stronger atmospheric turbulence is, the larger $\left(\frac{D}{r_0}\right)$ is.

A set of Zernike coefficients was acquired using the method we discussed above with the condition of $\frac{D}{r_0} = 20$. We simulated the distorted wavefront under strong atmospheric turbulence conditions by adjusting the deformable mirror to generate a set of aberrations. We then used the checkerboard algorithm and the
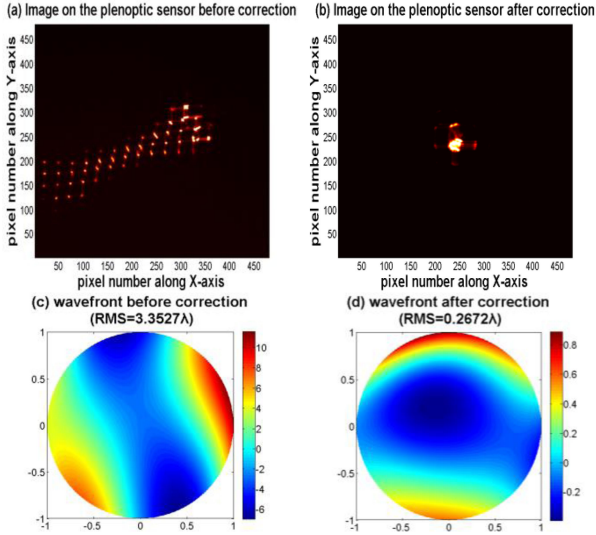
Fig. 19. Wavefront correction result of strong turbulence using checkerboard algorithm.
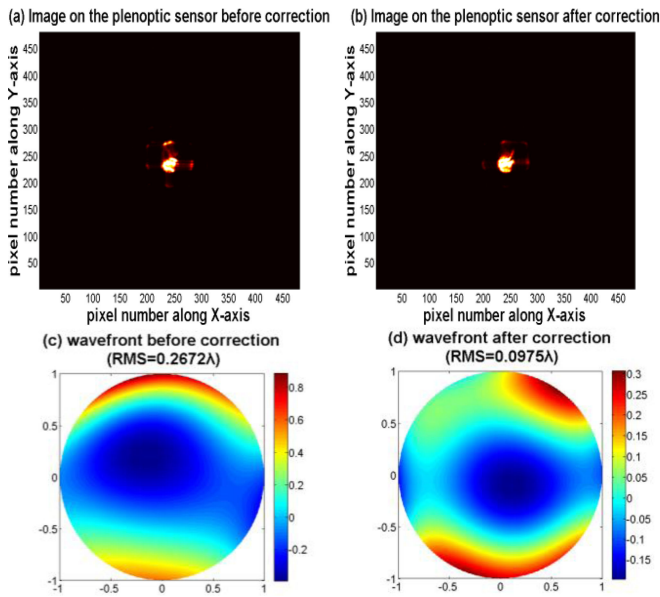

Fig. 20. Residual wavefront correction result using LTC algorithm.

direct-gradient method to perform wavefront reconstruction and correction, respectively, on the distorted wavefront. Fig. 19(a) and 19(b) show the plenoptic sensor imaging before and after correction, the corrected incident beam was mostly concentrated on the central MLA sub-aperture, Strehl ratio was improved from 0.032 to 0.362 after correction with checkerboard algorithm. Fig. 19(c) and 19(d) show the wavefront before and after correction, The wavefront RMS values before and after correction are 3.3527 λ, and 0.2672 λ, respectively, and the P-V values are 17.2013 λ, and 1.3683 λ, respectively, which means that most of the aberrations have been corrected. However, there still remains nearly 0.2 λ of the Defocus and 0.15 λ of the Astigmatism aberrations. As already discussed, owing to the limitation of

the checkerboard algorithm itself, it is difficult to correct the residual aberrations using only the checkerboard algorithm.

To further improve the accuracy of wavefront correction, after the closed-loop correction of the distorted wavefront, the LTC algorithm and the direct-gradient method were used to reconstruct and correct the residual aberrations. The wavefront correction result of LTC algorithm is shown in Fig. 20, where Fig. 20(a) is the plenoptic sensor imaging before correction, and Fig. 20(b) is that after correction. More incident beam was concentrated in the central MLA sub-aperture, and Strehl ratio was improved from 0.362 to 0.711 after correction with LTC algorithm. Fig. 20(c) and (d) are the wavefront before and after correction. The wavefront RMS values before and after correction are 0.2672 λ and 0.0975 λ, respectively, and the P-V values are 1.3683 λ and 0.8671 λ, respectively. After using the LTC algorithm, the residual aberration is further reduced, and a higher correction accuracy is obtained.

IV. CONCLUSION

In this study, a local threshold checkerboard algorithm based on the plenoptic sensor is proposed. Compared with the original algorithm, our algorithm amplifies the wavefront reconstruction results of the residual aberrations by thresholding specific areas in the central sub-aperture, which can improve the accuracy of wavefront reconstruction. An experimental platform is designed and built to verify the effectiveness of the algorithm. Experimental results showed that our algorithm can effectively improve the accuracy of wavefront reconstruction. Moreover, we used the direct-gradient method to effectively correct the residual aberrations

REFERENCES

[1] H. W. Babcock, "The possibility of compensating astronomical seeing," *Pub. Astronomical Soc. Pacific*, vol. 65, no. 386, pp. 229–236, 1953 doi: 10.1086/126606.
[2] R. K. Tyson, *Principles of Adaptive Optics*, 3rd ed. Boca Raton, FL, USA: CRC Press, 2010.
[3] X. Zhang *et al.*, "First light on the 127-element adaptive optical system for 1.8-m telescope," *Chin. Opt. Lett.*, vol. 8, no. 11, pp. 1019–1021, 2018.
[4] A. T. Watnik and D. F. Gardner, "Wavefront sensing in deep turbulence," *Opt. Photon. News*, vol. 29, no. 10, pp. 38–45, 2018, doi: 10.1364/OPN.29.10.000038.
[5] P. Jiang *et al.*, "Comparison of the Shack-Hartmann and plenoptic sensor in closed-loop adaptive optics system," *Opt. Eng.*, vol. 55, no. 3, pp. 033105, 2016, doi: 10.1117/1.OE.55.3.033105.
[6] J. Rodríguez-Ramos *et al.*, "Wavefront and distance measurement using the CAFADIS camera," *Adaptive Opt. Syst.*, vol. 7015, 2008, Art. no. 70155Q.
[7] C. Wu and C. C. Davis, "Modified plenoptic camera for phase and amplitude wave front sensing," *Laser Commun. Propag. Through Atmos. Oceans II*, vol. 8874, 2013, Art. no. 88740I.
[8] C. Wu *et al.*, "Phase and amplitude wave front sensing and reconstruction with a modified plenoptic camera," *Laser Commun. Propag. through Atmos. Oceans III*, vol. 9924, 2014, Art. no. 92240G.
[9] C. Wu *et al.*, "Determining the phase and amplitude distortion of a wavefront using a plenoptic sensor," *J. Opt. Soc. Amer. A Opt. Image Sci. Vis.*, vol. 32, no. 5, pp. 964–978, 2015, doi: 10.1364/JOSAA.32.000964.

[10] C. Wu *et al.*, "Complex wave front sensing with a plenoptic sensor," *Laser Commun. Propag. through Atmos. Oceans V*, vol. 9979, 2016, Art. no. 99790Y.

[11] C. Wu *et al.*, "Plenoptic mapping for imaging and retrieval of the complex field amplitude of a laser beam," *Opt. Exp.*, vol. 24, no. 26, pp. 29852–29871, 2016, doi: 10.1364/OE.24.029852.

[12] C. Wu *et al.*, "Imaging through strong turbulence with a light field approach," *Opt. Exp.*, vol. 24, no. 11, pp. 11975–11986, 2016, doi: 10.1364/OE.24.011975.

[13] C. Wu *et al.*, "Using a plenoptic sensor to reconstruct vortex phase structures," *Opt. Lett.*, vol. 41, no. 14, pp. 3169–3172, 2016, doi: 10.1364/OL.41.003169.

[14] J. Ko and C. C. Davis, "Comparison of the plenoptic sensor and the Shack-Hartmann Sensor," *Appl. Opt.*, vol. 56, no. 13, pp. 3689–3698, 2017, doi: 10.1364/AO.56.003689.

[15] C. Wu *et al.*, "Comparison between the plenoptic sensor and the light field camera in restoring images through turbulence," *OSA Continuum*, vol. 2, no. 9, pp. 2511–2525, 2019, doi: 10.1364/OSAC.2.002511.

[16] J. Ko *et al.*, "An adaptive optics approach for laser beam correction in turbulence utilizing a modified plenoptic camera," in *Proc. Laser Commun. Propag. through Atmos. Oceans IV*, vol. 9614, 2015, Art. no. 96140I.

[17] J. Hu *et al.*, "Improved wave-front reconstruction and correction strategy for adaptive optics system with a Plenoptic sensor," *IEEE Photon. J.*, vol. 13, no. 4, Aug. 2021, Art. no. 6801008.

[18] E. P. Wallner, "Optimal wave-front correction using slope measurements," *JOSA*, vol. 73, no. 12, pp. 1171–1176, 1983.

[19] X. Li *et al.*, "Zernike modal compensation analysis for an adaptive optics system using direct-gradient wave-front reconstruction algorithm," *Adapt. Opt. Syst. Technol.*, vol. 3762, pp. 116–124, 1999.

[20] X. Li and W. Jiang, "Comparing zonal reconstruction algorithms and modal reconstruction algorithms in adaptive optics system," *High-Resolution Wavefront Control: Methods, Devices, Appl. IV*, vol. 4825, 2002, pp. 121–130.

[21] N A. Roddier, "Atmospheric wavefront simulation using Zernike polynomials," *Opt. Eng.*, 1990, vol. 29, no. 10, pp. 1174–1180.